Biosensors and Bioelectronics 200 (2022) 113899

Contents lists available at ScienceDirect

Biosensors and Bioelectronics

journal homepage: www.elsevier.com/locate/bios

Construction of a highly selective and sensitive carbohydrate-detecting biosensor utilizing Computational Identification of Non-disruptive Conjugation sites (CINC) for flexible and streamlined biosensor design

Dustin D. Smith [a,b], Dylan Girodat [a,b,1], D. Wade Abbott [b,c], Hans-Joachim Wieden [a,b,d,2,*]

[a] Alberta RNA Research and Training Institute (ARRTI), University of Lethbridge, Lethbridge, AB, Canada
[b] Department of Chemistry and Biochemistry, University of Lethbridge, Lethbridge, AB, Canada
[c] Lethbridge Research and Development Centre, Agriculture and Agri-Food Canada, Lethbridge, AB, Canada
[d] Department of Microbiology, University of Manitoba, Winnipeg, MB, Canada

ARTICLE INFO

Keywords:
Computational biosensor design
Molecular dynamics
Fluorescence
Rapid kinetics
MalX
Carbohydrate detection

ABSTRACT

Fluorescently-labeled solute-binding proteins that alter their fluorescence output in response to ligand binding have been utilized as biosensors for a variety of applications. Coupling protein ligand binding to altered fluorescence output often requires trial and error-based testing of both multiple labeling positions and fluorophores to produce a functional biosensor with the desired properties. This approach is laborious and can lead to reduced ligand binding affinity or altered ligand specificity. Here we report the Computational Identification of Non-disruptive Conjugation sites (CINC) for streamlined identification of fluorophore conjugation sites. By exploiting the structural dynamics properties of proteins, CINC identifies positions where conjugation of a fluorophore results in a fluorescence change upon ligand binding without disrupting protein function. We show that a CINC-developed maltooligosaccharide (MOS)-detecting biosensor is capable of rapid (k_{on} = 20 $\mu M^{-1}s^{-1}$), sensitive (sub-μM K_D) and selective MOS detection. The MOS-detecting biosensor is modular with respect to the spectroscopic properties and demonstrates portability to detecting MOS released via α-amylase-catalyzed depolymerization of starch using both a stopped-flow and a microplate reader assay. Our MOS-detecting biosensor represents a first-in-class probe whose design was guided by changes in localized dynamics of individual amino acid positions, supporting expansion of the CINC pipeline as an indispensable tool for a wide range of protein engineering applications.

1. Introduction

Biosensors are devices that utilize biological components to detect the presence or amount of molecules of interest and give a quantifiable output (Mehrotra, 2016). The market value for biosensors in 2019 was US$ 21.2 billion and is projected to exceed US$ 31.5 billion by 2024 (Markets and Markets, 2019). These projections are derived from the impact that biosensors have on, but are not limited to, medicine, agriculture, environmental monitoring, biofuels, and academic research (Harrison and Dunlop, 2012; Ispas et al., 2012; Law et al., 2015; Mehrotra, 2016; Pardee et al. 2014, 2016; Rai et al., 2012; Shin, 2011; Srilatha, 2011; Verma and Bhardwaj, 2015). As such, the opportunity to develop novel biosensors capable of specific and sensitive monitoring of compounds at low concentrations and with high dynamic range is growing rapidly (Edwards, 2021; Yu et al., 2021; Zeng et al., 2021; Zhang et al. 2018a, 2018b). A general approach to biosensor development is the conjugation of fluorophores to a particular protein that binds a specific molecule of interest. This approach utilizes the innate specificity and affinity that proteins possess for their ligands and exploits fluorescence signal changes induced upon protein-ligand interactions. Protein-fluorophore conjugates have been used as anion or cation-detecting biosensors (Belousov et al., 2006; Chen et al., 2013; De Lorimier et al., 2002; Smith et al., 2017; Solscheid et al., 2015), nucleotide-detecting biosensors (Berg et al., 2009; Bianchi-Smiraglia et al., 2017; Kunzelmann and Webb, 2010), amino acid detecting biosensors (Ciftci et al., 2020; De Lorimier et al., 2002; Ko et al. 2016,

* Corresponding author. Alberta RNA Research and Training Institute (ARRTI), University of Lethbridge, Lethbridge, AB, Canada.
E-mail address: hans-joachim.wieden@umanitoba.ca (H.-J. Wieden).
[1] Current address: Theoretical Biology and Biophysics Group, Theoretical Division, Los Alamos National Laboratory, Los Alamos, NM, United States of America.
[2] Current address: Department of Microbiology, University of Manitoba, Winnipeg, MB, Canada.

https://doi.org/10.1016/j.bios.2021.113899
Received 21 September 2021; Received in revised form 18 November 2021; Accepted 16 December 2021
Available online 20 December 2021

2017), and carbohydrate detecting biosensors (De Lorimier et al., 2002; Fonin et al., 2014; Hsieh et al., 2012; Marvin et al., 2011; Tian et al., 2007). The development of biosensors often involves fluorophore labeling near the ligand binding site, exploiting ligand binding events to induce a change in the local in environment proximal to the conjugated fluorophore (e.g., as in (Brune et al., 1994; De Lorimier et al., 2002; Gilardi et al., 1994)). However, introducing a fluorescent label in the vicinity of the ligand binding site can perturb the activity of the resulting protein-conjugate, reducing binding affinity or specificity for the respective ligand (Brune et al., 1994; De Lorimier et al., 2002; Gilardi et al., 1994; Toseland, 2013). Altogether, stochastic approaches can be expensive, laborious, time consuming and unsuccessful; thus, the development of an *in silico* screening step for selection of non-disruptive fluorophore conjugation sites would accelerate the design and development of new biosensors.

Previous findings by our group have highlighted how binding of small ligands to their respective proteins, such as EF-Tu and YchF, can alter the localized dynamics of amino acids distal from the ligand binding site (De Laurentiis et al., 2016; Girodat et al., 2019; Mercier et al., 2015; Rosler et al., 2015). The localized structural dynamics responses of amino acids gleaned from these investigations enabled our establishment of a computational pipeline, entitled Computational Identification of Non-disruptive Conjugation sites (CINC), to predict and exploit these changes as generation principles for identification of fluorophore conjugation sites on structurally unrelated proteins. More specifically, we identify how the structural dynamics properties of amino acids are altered upon ligand binding, producing localized environmental changes which can be detected by a conjugated fluorophore distal from the ligand binding site. This approach examines the localized structural dynamics properties of a protein of interest with amino acid resolution through molecular dynamics simulations of the *apo* and ligand-bound states followed by scoring each amino acid position with respect to changes in local dynamics. Our CINC pipeline examines several criteria proposed to influence fluorescence of environmentally-sensitive fluorophores (Fu and Finney, 2018; Marvin et al. 2011, 2019; Rurack and Resch-Genger, 2002). Additionally, we have considered the proximity of amino acids with regards to tryptophan residues, enabling access to Förster Resonance Energy Transfer (FRET)-based biosensors via introduction of a fluorophore capable of forming a tryptophan FRET pair. As a proof of concept, we report the development of a biosensor using the CINC pipeline to engineer the MalX protein from *Streptococcus pneumoniae* (Abbott et al., 2010) for specific, continuous, and direct detection of maltooligosaccharides (MOS). Our approach is not limited to ligand binding and in principle is applicable to any protein that undergoes localized structural dynamics changes as a function of pH, oxidation, temperature, or other factors that influence small scale structural dynamics. In summary, the CINC pipeline is a rapid, unbiased *in silico* screening step for engineering novel protein-fluorophore conjugates. We envision CINC having a transformative role in applications where rapid and automated engineering of diverse biosensor sets is required, for example, in the design of carbohydrate-detecting biosensors which to date have a detecting specific set of tools capable of detection of specific carbohydrates.

2. Materials and methods

2.1. Computational Identification of Non-disruptive conjugation sites (CINC), molecular dynamics simulations

Structural models of MalX in its *apo* and MOS-bound state were obtained from protein data bank (2XD2 and 2XD3, respectively (Abbott et al., 2010);) and used for molecular dynamics simulations. Following the approach established in our previous studies (De Laurentiis et al., 2016; Girodat et al., 2019; Mercier et al., 2015; Rosler et al., 2015), each model of the protein was solvated with a TIP3P water box extending 20 Å from any point on the protein and brought to a concentration of 100 mM NaCl. The potential energy of the water and then the entire system was minimized using AMBER FF99SB force fields for 10 000 steps each. The system was equilibrated and subsequently heated to 300K for 10 000 steps each. Finally, molecular dynamics simulations were performed for 100 ns at a step size of 2 fs using Langevin dynamics to maintain temperature at 300K. The root-mean squared deviation (RMSD) for both *apo* and MOS-bound states remained stable after an initial equilibration of 10 ns at values of ~2.5 Å and ~4 Å respectively (Fig. S1).

2.2. F_{Score}

Trajectories from each simulation were put through the CINC pipeline where the backbone flexibility, backbone dihedral angles, distance to ligand, distance to tryptophan residues, and solvent accessibility were measured to develop a ranking score (F_{Score}, Fig. 1A). These properties were chosen as localized dynamic features of an amino acid that would have the largest impact on the environment of the conjugated fluorophore. Only amino acids with a conservation score of 1 from the ConSurf server (Ashkenazy et al., 2016; Celniker et al., 2013) and that are further than 5 Å away from the ligand binding site were assigned an F_{Score} to ensure there would be no impact on ligand binding properties (Fig. 1B). Flexibility was determined by measuring the root-mean-square fluctuation (RMSF) of the Cα atoms of each amino acid over the course of both the ligand bound (F_{Lr}) and *apo* (F_{Ar}) simulations (Eq. (1)). Backbone dihedral angles were measured by determining the φ (between atoms C–N-Cα-C) or ψ (between atoms N-Cα-C-N) angles and then using these angles to construct a Ramachandran plot. The Ramachandran plot was then transformed into a 180 × 180 matrix (Fig. 1C and D) and the sum of the difference between the matrices for the ligand bound (B_{Lr}) and *apo* (B_{Ar}) conformation was used to determine the conformational change in the backbone dihedrals at that residue (Eq. (1)). Distances from each amino acid to the ligand were measured for the ligand bound simulation (L_{Lr}) directly, whereas the structure of the ligand bound conformation was aligned to the *apo* simulation to measure the distance from each amino acid to the ligand (L_{Ar}) (Eq. (1)). Tryptophan distances were measured for both ligand-bound (T_{Lr}) and *apo* (T_{Ar}) (Eq. (1)). In circumstances where there is more than one tryptophan the distances between an amino acid and each tryptophan were averaged to obtain an average amino acid to tryptophan distance. Last, the solvent accessibility of each amino acid was determined and compared between the ligand bound (S_{Lr}) and *apo* (S_{Ar}) conformations (Eq. (1)). The values measured were averaged and the absolute value | | of the difference between ligand bound and *apo* conformations was normalized compared to the maximum (v) value obtained (Eq. (1)). Using this approach each amino acid that was under consideration could be assigned an F_{score} from 0 to 5, with a higher score indicating a better candidate for fluorophore conjugation.

$$\boldsymbol{F}_{score}=\frac{|\langle \boldsymbol{S}_{Lr}\rangle-\langle \boldsymbol{S}_{Ar}\rangle|}{\mathrm{v}|\langle \boldsymbol{S}_{Lr}\rangle-\langle \boldsymbol{S}_{Ar}\rangle|}+\frac{|\langle \boldsymbol{T}_{Lr}\rangle-\langle \boldsymbol{T}_{Ar}\rangle|}{\mathrm{v}|\langle \boldsymbol{T}_{Lr}\rangle-\langle \boldsymbol{T}_{Ar}\rangle|}+\frac{|\langle \boldsymbol{L}_{Lr}\rangle-\langle \boldsymbol{L}_{Ar}\rangle|}{\mathrm{v}|\langle \boldsymbol{L}_{Lr}\rangle-\langle \boldsymbol{L}_{Ar}\rangle|}+\frac{|\langle \boldsymbol{F}_{Lr}\rangle-\langle \boldsymbol{F}_{Ar}\rangle|}{\mathrm{v}|\langle \boldsymbol{F}_{Lr}\rangle-\langle \boldsymbol{F}_{Ar}\rangle|}+\frac{\sum|[\boldsymbol{B}_{Lr}]-[\boldsymbol{B}_{Ar}]|}{\mathrm{v}\sum|[\boldsymbol{B}_{Lr}]-[\boldsymbol{B}_{Ar}]|} \quad (1)$$

2.3. Biosensor construct design

All MalX variants were engineered to lack the signal secretion peptide and lipoprotein attachment motif found in wild-type *malX* (*Streptococcus pneumoniae*) as previously described (Abbott et al., 2010). *malX* variants were synthesized with flanking 5′ *NheI* and 3’ *XhoI* restriction sites and subcloned into pET28a yielding pET28a:*malX A134C*, pET28a:*malX A180C,* pET28a:*malX T249C,* and pET28a:*malX E318C* (BioBasic Canada Inc.). Criteria for selection of these variants was guided by the CINC pipeline and is explained in detail in Section 3.2. All constructs encoded an N-terminal poly-Histidine tag fusion.

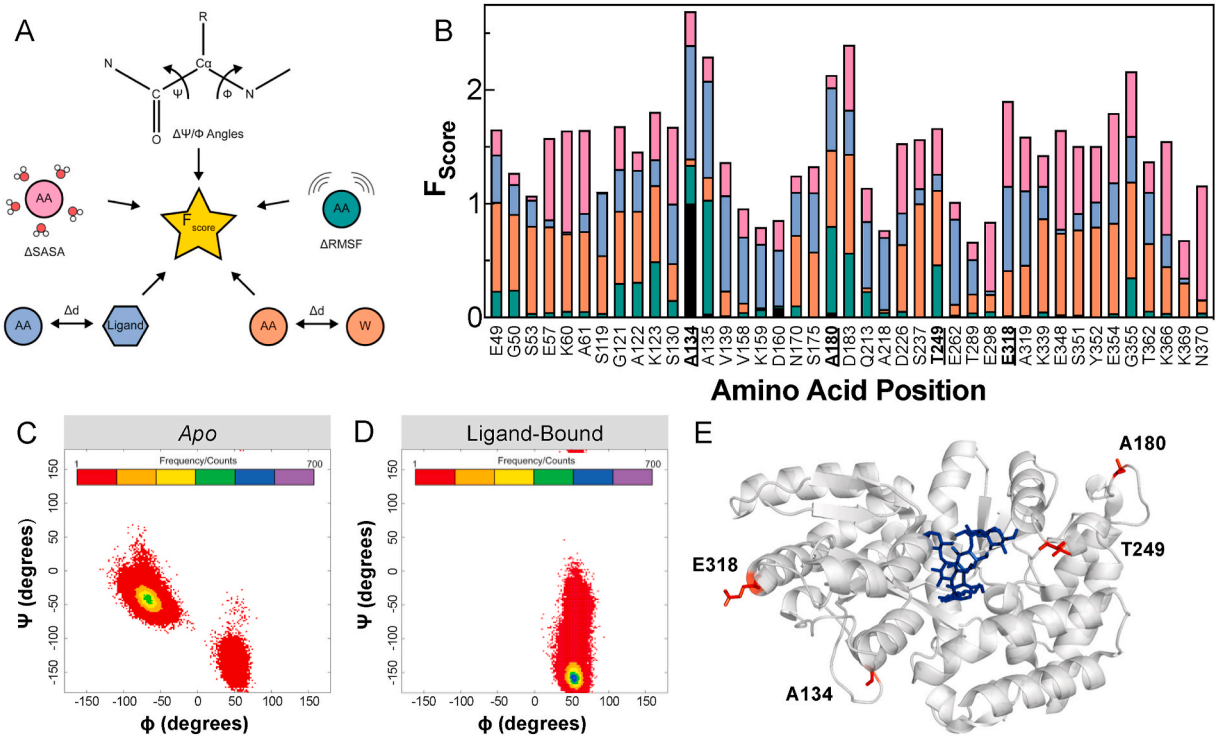

Fig. 1. Overview of CINC-based design of MOS-detecting biosensors based on MalX using 100 ns molecular dynamics simulations. (A) Overview of factors that contribute to the F_{Score} of an amino acid position. (B) F_{Score} values and the contributions of individual factors for candidate labeling positions in MalX. Shown are changes in backbone dihedral angles (black), in RMSF (green), in the distance to Trp (orange), in the distance to the ligand (blue), and changes in solvent accessible surface (pink). Ramachandran plot for position A134 from 100 ns *apo* (C) or ligand-bound (D) molecular dynamics simulations of MalX. (E) Candidate substitution positions (red) A134, A180, T249, and E318 and their location in MOS-bound MalX (PDB 2XD3, figure generated using PyMOL). (For interpretation of the references to colour in this figure legend, the reader is referred to the Web version of this article.)

2.4. Expression of MalX variants

Escherichia coli BL21(DE3) gold cells (Agilent) transformed with either pET28a:*malX A134C*, pET28a:*malX A180C,* pET28a:*malX T249C,* or pET28a:*malX E318C* were used to inoculate LB media (10 g/L typtone, 5 g/L yeast extract, 10 g/L NaCl) supplemented with 50 mg/L kanamycin to an optical density at 600 nm (OD_{600}) ≈ 0.1. After growth at 37 °C with 200 RPM shaking, isopropyl β-D-1-thiogalactopyranoside (IPTG) was added to a final concentration of 1 mM when OD_{600} reached approximately 0.6. Cultures were grown for an additional 3 h, cells harvested by centrifugation (5000×*g*, 10 min, 4 °C), flash frozen, and stored at −80 °C for further use.

2.5. Purification of MalX variants

Cell pellets were resuspended in 7 mL/g of Buffer A (20 mM Tris pH 8.0 at 4 °C, 0.5 M NaCl, 10 mM imidazole, 7 mM β-mercaptoethanol, 1 mM phenylmethylsulfonylfluoride), and lysozyme added to a final concentration of 1 mg/mL prior to a 30-min incubation at 4 °C. Sodium deoxycholate was added to a final concentration of 12.5 mg per gram of cells, and the suspension was sonicated (Branson Sonifier 450) on ice for 1 min at 50% output and 60% duty cycle (repeated twice, with a 5 min break between cycles). The resulting lysate was centrifuged (3000×*g*, 30 min, 4 °C) to pellet insoluble debris, followed by additional centrifugation to produce S30 extract (30 000×*g*, 45 min, 4 °C). The obtained S30 extract was applied to Ni^{2+}-Sepharose resin in a batch-chromatography setup (3 mL resin per 1 g of cells opened) and incubated for 30 min at 4 °C. Ni^{2+}-Sepharose resin was collected by centrifugation (500×*g*, 2 min, 4 °C), and supernatant decanted. The collected Ni^{2+}-Sepharose resin was washed 3 times with 10 resin-volumes of Buffer A, followed by 4 washes with 10 resin-volumes Buffer B (Buffer A with 20 mM imidazole). Bound protein was eluted six times with 1 resin-volume Buffer C (Buffer A with 250 mM imidazole). Samples were analyzed via sodium dodecyl sulfate polyacrylamide gel electrophoresis (SDS-PAGE) stained with Coomassie Brilliant Blue, and fractions containing each MalX variant were pooled and dialyzed at 4 °C into Buffer D for labeling (20 mM Tris pH 7.5 @ 20 °C, 0.5 M NaCl, 30 mM imidazole, 20 mL sample into 1 L Buffer D, dialysis tubing molecular weight cut-off 12.4 kDa, 3 changes). Purified protein was flash-frozen with liquid nitrogen and stored at −80 °C for further use. Purification yields were typically 100 mg of protein per liter of culture.

2.6. Fluorescent labeling of MalX variants

Labeling reactions were performed essentially as described previously (Smith et al., 2017). The respective MalX variants (100 μM concentration in labeling reaction, 15 mL reaction volume) were incubated with 3.5 mL Ni^{2+}-Sepharose resin in Buffer D. Five-fold molar excess of either 7-diethylamino-3-(4′-maleimidylphenyl)-4-methylcoumarin (CPM, from 20 mM stock in dimethyl sulfoxide (DMSO), Biotium), *N*-(7-dimethylamino-4-methylcoumarin-3-yl)maleimide (DACM, from 20 mM stock in dimethylformamide (DMF), Invitrogen), *N*-[2-(dansylamino)ethyl]maleimide (Dansyl, from 25 mM stock in DMSO, Sigma Aldrich), fluorescein-5-maleimide (Fluorescein, from 50 mM stock in DMSO, Biotium), 7-diethylamino-3-[*N*-(2-maleimidoethyl)carbamoyl] coumarin (MDCC, from 20 mM stock in DMF, Sigma Aldrich), *N*-(1-pyrene)maleimide (Pyrene, from 20 mM stock in DMF, Sigma Aldrich), or Rhodamine Red C2 maleimide (Rhodamine Red, from 20 mM stock in DMF, Invitrogen) was added dropwise to the labeling mixture corresponding to a final concentration of 500 μM in the labeling reaction. The labeling reaction was subsequently incubated on an end-over-end mixer at room temperature for 2 h, followed by 12 h at 4 °C. Ni^{2+}-Sepharose resin was collected by centrifugation (500×*g*, 2 min, 4 °C) and the supernatant decanted. The resin was washed six times

with three resin-volumes of Buffer D, followed by six elutions with Buffer E (Buffer D with 250 mM imidazole). Labeling procedure samples were analyzed via SDS PAGE, and the respective gels visualized under UV light (312 nm) or stained using Coomassie Brilliant Blue. Fractions containing labeled MalX were pooled and dialyzed into 50 mM Tris pH 7.5 @ 20 °C (20 mL sample in 1 L Buffer, 4 changes, molecular weight cut-off 12.4 kDa). The protein recovery from the labeling procedure was ~50% and labeling efficiencies were typically 70% to >90%. Concentration of labeled MalX variants were calculated as described below (Eq. (2) and (3)) using the following parameters: 0.164 as a correction factor accounting for MDCC absorption at 280 nm (Brune et al., 1994; Smith et al., 2017), $\varepsilon_{280,\ MalX} = 61\ 310\ M^{-1}\ cm^{-1}$ is the calculated extinction coefficient based on protein primary sequence (Gasteiger et al., 2005), L is instrument path length in cm, and $\varepsilon_{430,\ MDCC} = 46\ 800\ M^{-1}cm^{-1}$ (Brune et al., 1994; Smith et al., 2017). MalX A134C-MDCC and MalX T249C-MDCC Biosensor preparations are currently available from Allos Bioscience Ltd. (B1001 and B1002 respectively).

$$[MalX\ variant] = \frac{A_{280} - (A_{430} \times 0.164)}{\varepsilon_{280,\ MalX} \times L} \quad (2)$$

$$[MDCC] = \frac{A_{430}}{\varepsilon_{430,\ MDCC} \times L} \quad (3)$$

Protein concentration for MalX A134C-CPM, MalX A134C-DACM, MalX A134C-Dansyl, MalX A134C-Fluorescein, MalX A134C-Pyrene, and MalX A134C-Rhodamine Red were determined via densitometry analysis (ImageJ (Schneider et al., 2012)) of SDS-PAGE gels using MalX A134C-MDCC samples to form a standard curve. Concentrations of the respective conjugated fluorescent labels were calculated from spectroscopic data by modifying Equation (3) using the appropriate wavelength and manufacturer provided extinction coefficients: $\varepsilon_{384,\ CPM} = 33\ 000\ M^{-1}cm^{-1}$, $\varepsilon_{384,\ DACM} = 27\ 000\ M^{-1}cm^{-1}$, $\varepsilon_{340,\ Dansyl} = 4300\ M^{-1}cm^{-1}$, $\varepsilon_{494,\ Fluorescein} = 68\ 000\ M^{-1}cm^{-1}$, $\varepsilon_{339,\ Pyrene} = 38\ 000\ M^{-1}cm^{-1}$, $\varepsilon_{560,\ Rhodamine\ Red} = 119\ 000\ M^{-1}cm^{-1}$. Labeling efficiencies for all protein-fluorophore conjugates were determined using Equation (4).

$$Labeling\ efficiency = \frac{[Fluorophore]}{[MalX\ A134C]} \times 100\% \quad (4)$$

2.7. Carbohydrates and α-amylase

Maltotriose (M3) was purchased from Megazyme (O-MAL3); isomaltotriose was purchased from Carbosynth (OI05352); maltose (M5885), maltoheptaose (M7753), water soluble starch (S9765), and *Bacillus licheniformis* α-amylase (A3403) were purchased from Sigma Aldrich.

2.8. Equilibrium fluorescence experiments

Fluorescence spectrophotometry was performed using a Quanta Master 60 Fluorescence Spectrometer (Photon Technology International, all experiments utilized 1 nm step size, 1 s integration). For experiments in Fig. 2, excitation slit widths were 1 nm, emission slit widths were 2 nm, excitation wavelength was 420 nm, and emission wavelength was 425–575 nm. For data presented in Fig. 3, excitation and emission wavelengths were the same as in Fig. 2, except excitation slit widths were 4 nm, emission slit widths were 8 nm. To obtain K_D, a hyperbolic function (Eq. (5)) was fit to the data in GraphPad Prism v. 9.0, where Y is the absolute value of the fluorescence change at each [M3], B_{max} is the maximum specific binding in the same units as Y extrapolated to very high ligand concentrations, and K_D is the equilibrium binding constant.

$$Y = \frac{B_{max} \times [M3]}{K_D + [M3]} \quad (5)$$

For data presented in Table S1 and Table S2, protein concentration

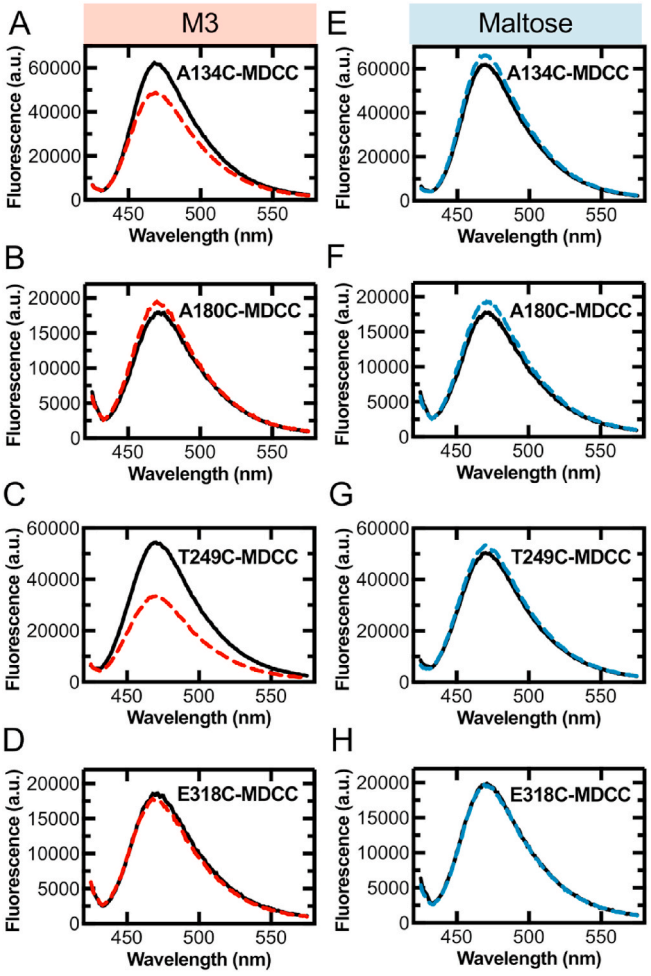

Fig. 2. Fluorescence spectra of MOS-detecting biosensors. MOS-detecting biosensor (1 μM) fluorescence in the absence (black solid line) and presence (red dashed line) of 20 μM M3 for (A) A134C-MDCC, (B) A180C-MDCC, (C) T249C-MDCC, and (D) E318C-MDCC. MOS-detecting biosensor in the absence (black solid line) and presence (blue dashed line) of 30 μM maltose for (E) A134C-MDCC, (F) A180C-MDCC, (G) T249C-MDCC, and (H) E318C-MDCC. (For interpretation of the references to colour in this figure legend, the reader is referred to the Web version of this article.)

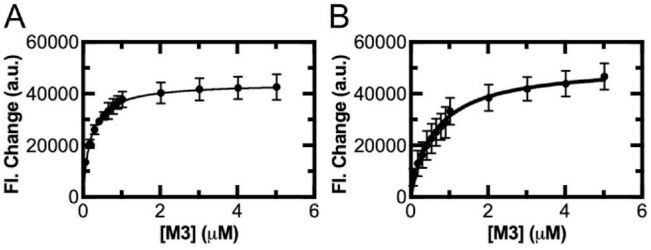

Fig. 3. Concentration dependence of M3-binding induced fluorescence change in MOS-detecting biosensors. MOS-detecting biosensor (20 nM) binds M3 with an affinity of (A) A134C-MDCC, 190 ± 50 nM and (B) T249C-MDCC, 600 ± 200 nM (n = 13 data points, best fit ± 95% c. i.) demonstrating the high sensitivity of the biosensor.

was 20 nM (except the MalX A134C-Dansyl conjugate, which was assayed at 1 μM due to lower extinction coefficient). Emission spectra were generally recorded in windows of 150 nm and included the designated Table S2 emission maxima wavelengths. **ΔI** was determined as follows:

$$\Delta I = \frac{maximum\ emission\ (MOS\ bound) - maximum\ emission\ (apo)}{maximum\ emission\ (apo)} \times 100\% \quad (6)$$

2.9. Rapid-kinetics measurements

Rapid kinetics experiments were performed using a KinTek SF-2004 stopped-flow apparatus (KinTek Corp.) at 20 °C. An excitation wavelength of 420 nm was used for all rapid kinetics experiments, and fluorescence emission was measured after passing a 450 nm long-pass filter. Individual fluorescence time-courses were fit with a one exponential function (Eq. (7)), where F is fluorescence observed at time t, F_∞ is final fluorescence, A is signal amplitude, and k_{app} is apparent rate (TableCurve, Systat Software).

$$F = F_\infty + A_1 \times \exp(-k_{app}t) \quad (7)$$

2.10. Microplate reader experiments

Microplate reader experiments were performed using a SpectraMax i3x plate reader (Molecular Devices, Fluorescence: Kinetic mode, 420 nm excitation (9 nm range), 465 nm emission (15 nm range), PMT gain: high, 6 flashes per read, sampling interval: 1 min) in a 96 well plate. Individual fluorescence time-courses were fit using a one-exponential function as described in Section 2.9 (Eq. (7)), and data was plotted using GraphPad Prism v. 9.0.

3. Results

3.1. Overview

As a proof-of-concept for the CINC pipeline we sought to develop a highly specific and sensitive biosensor for the study of Carbohydrate Active Enzymes (CAZymes). CAZymes are a group of sequence-diverse enzyme families belonging to five different functional classes that modify the linkages or decorations of carbohydrates (Lombard et al., 2013). CAZymes are commonly used in bioindustrial processes, including biofuel production, food processing, and textile finishing (Polaina and MacCabe, 2007). In this context, we chose MalX from *Streptococcus pneumoniae* as a candidate for the specific, continuous, and direct detection of MOS (Webb et al., 2008). MOS are oligosaccharides comprised of glucose molecules linked via α-1,4-glycosidic linkages. MalX is a lipid-anchored solute-binding protein (SBP) of an ATP binding cassette (ABC) transporter responsible for the selective transport of MOS produced by extracellular debranching of amylopectin by SpuA (Abbott et al., 2010). MalX binds MOS with a degree of polymerization between 3 and 8 ($K_D \sim 1$ μM), and accommodates MOS with degree of polymerization of 9–11 (Abbott et al., 2010). Structural studies of MalX indicate that MOS binding occurs at an interface between the N- and C-terminal domains similar to other SBP-ligand interactions, and MOS binding stabilizes a hinge-bend motion where the two domains move towards each other (Abbott et al., 2010). Together, these properties of MalX made it a promising candidate for the development of a MOS-detecting biosensor. Unlike previous biosensor design approaches that exploit global protein conformational changes in response to ligand binding, we utilized the CINC pipeline to identify labeling positions based on localized altered dynamics of individual amino acid positions, limiting the impact on protein function.

3.2. Selection of fluorophore conjugation sites in MalX using CINC

The CINC pipeline was used to rank-select optimal fluorophore conjugation sites in MalX for development of a novel MOS-detecting biosensor. The CINC pipeline was developed to take into consideration structural dynamics features of amino acids that differ between two distinct states. The properties selected were RMSF, solvent accessible surface area, backbone flexibility, and distance to ligand or tryptophan (Fig. 1A). To obtain information regarding changes in the local structural dynamics of each amino acid position in MalX, both the *apo* and MOS-bound MalX states were each subjected to 100 ns molecular dynamics simulations and candidate amino acid positions were assigned an F_{Score} score using the CINC pipeline. Amino acids were considered candidates if they were given a Consurf score of 1, indicating lack of sequence conservation (Ashkenazy et al., 2016; Celniker et al., 2013), to avoid modification of potentially functionally relevant amino acids (Fig. 1B). From the F_{Score} data we chose four positions to substitute with cysteine and to subsequently conjugate with a thiol-reactive fluorophore. Positions A134 and A180 were selected as two of the highest overall scorers (F_{Score} 2.7 and 2.0 respectively), and positions T249 and E318 (F_{Score} 1.6 and 1.9 respectively) were chosen as mid-level scorers to test the robustness of F_{Score} (Fig. 1B–E). Of these labeling positions, the strongest contributor to F_{score} for each mutant were changes in backbone dihedral angles (A134), changes in RMSF (A180), distance to Trp (T249), and change in proximity to ligand/solvent accessible surface area (E318) – these variants can therefore be used to examine the predictive power of these parameters in the F_{score} algorithm (Fig. 1B–E).

3.3. Candidate biosensor response to M3, fluorescence spectrophotometry

To perform initial screening, each of the four MalX variants were conjugated with MDCC, a diethylaminocoumarin previously used in the construction of other SBP-based biosensors (Brune et al., 1994; Hanes et al., 2011; Kunzelmann and Webb, 2009; Salins et al., 2002; Smith et al., 2017). Each MalX variant labeled with MDCC was examined using fluorescence spectrophotometry, directly measuring the change in fluorescence in response to M3 binding. The highest CINC scorer, A134, and a mid–CINC–scorer T249 exhibited a 20% and 30% fluorescence decrease upon binding of M3, respectively, whereas the MalX variants with MDCC conjugated at A180C and E318C did not exhibit a fluorescence change upon addition of M3 (Fig. 2A–D). In the presence of maltose as a ligand we observed little to no fluorescence change for all the variants, suggesting no binding (Fig. 2E–H, Fig. S2). The aforementioned result is consistent with previous data showing that three pyranose rings at the reducing end of a MOS are required to stabilize a protein-ligand complex with MalX via stacking interactions with aromatic amino acids at subsites 1–3 (Abbott et al., 2010). Therefore, MalX A134C-MDCC and MalX T249C-MDCC selectively detect M3 via a fluorescence change specific to MOS, confirming our initial hypothesis that changes in the local structural dynamics distant from the ligand binding site can be exploited for biosensor design. MalX A134C-MDCC also did not detect isomaltotriose, a compositionally similar carbohydrate to M3 whose α-1,6-glycosidic linkages create a spatially disposed conformation not recognized by MalX (Table S1, Fig. S2). A larger MOS, maltoheptaose, is detected by MalX A134C-MDCC, further demonstrating biosensor specificity for MOS (Table S1, Fig. S2). Labeling at positions 134 and 249 does not influence the ligand binding affinity of MalX, as equilibrium titration of each labeled protein with M3 revealed affinities (K_D) of 190 ± 50 nM and 600 ± 200 nM for MalX A134C-MDCC and MalX T249C-MDCC respectively (Fig. 3A and B), which are similar to the previously determined affinities of the unlabeled protein measured using UV difference spectroscopy (800 ± 125 nM), and Isothermal Titration Calorimetry (2.0 ± 0.2 μM) (Abbott et al., 2010). Altogether this demonstrates the robustness, sensitivity, and specificity our system for detecting and monitoring sub-μM concentrations of M3 without disruption of the ligand binding properties of wild-type MalX.

3.4. Real-time detection of M3 by MalX A134C-MDCC

To assess the ability of the biosensor developed using the CINC pipeline to detect binding in real-time we determined the kinetic parameters of M3 binding to MalX A134C-MDCC using the stopped-flow technique. In essence the stopped-flow apparatus used is a

fluorescence spectrophotometer coupled with a rapid mixing device, enabling real-time fluorescence measurements of rapid biomolecular events. Here, MalX A134C-MDCC was rapidly mixed with increasing concentrations of M3, and the resulting fluorescence time-courses representing binding of M3 to the biosensor were recorded. Consistent with first-order binding kinetics the obtained fluorescence time courses were best fit with a one-exponential function, yielding the total fluorescence change (A_1) and the apparent rate of binding (k_{app}) (Eq. (7)). Similar to the corresponding equilibrium fluorescence spectrophotometry data (see 3.3), rapid mixing of M3 and MalX A134C-MDCC resulted in a fluorescence decrease (Fig. 4A, Fig. S3). As the observed k_{app} increases with M3 concentration, the association rate constant (k_{on}) for M3 binding to MalX A134C-MDCC was determined from the slope of k_{app} as a function of the M3 concentration (Fig. 4B). The determined k_{on} of 20 ± 2 $\mu M^{-1}s^{-1}$ highlights the rapid M3 detection possible using our engineered biosensor. This further demonstrates that changes in the structural dynamics at sites distant from the ligand binding site can be used as rapid readout for the binding event and do not introduce delays. Rapid M3 detection by MalX A134C-MDCC makes the biosensor amenable to kinetic applications where M3 release is slower than detection by the biosensor (i.e. real-time detection of ligand formation by preceding enzymatic reaction). Interestingly, rapid kinetics analysis of M3 detection by MalX T249C-MDCC resulted in fluorescence time-courses that did not follow pseudo first-order binding kinetics and this biosensor was not utilized in rapid kinetics assays (data not shown) which further emphasizes the role of dihedral angle change as a key selection criterion for the labeling site. Although the complex kinetics observed with MalX T249C-MDCC make it less useful for real-time applications, this biosensor has utility in endpoint or equilibrium applications where sensitive MOS detection is required.

3.5. CINC-developed MalX A134C can be conjugated to a variety of fluorophores yielding biosensor with select spectroscopic properties

To examine the influence that the fluorophore species have on our CINC-developed biosensors, we conjugated MalX A134C to a variety of fluorophores with various structural and spectroscopic properties. Ultimately, we examined the impact of different fluorophore families (four) and linker compositions (three) (Fig. S4). To address linker composition, the coumarin fluorophores (CPM and DACM) were conjugated to MalX A134C and compared to the previously characterized MDCC conjugate. MDCC contains an N-ethylcarbamoyl linker between the coumarin and maleimide group, CPM contains a phenyl linker between the coumarin and maleimide group, and DACM contains no linker (Fig. S4). To examine the impact of fluorophore family on the MalX A134C-based biosensor Dansyl (naphthalene family), Fluorescein (xanthene family), Pyrene (pyrene family), and Rhodamine Red (xanthene family) were conjugated to MalX A134C and their response to a MOS examined (Fig. 5, Fig. S4, Table S2). Direct excitation of all tested

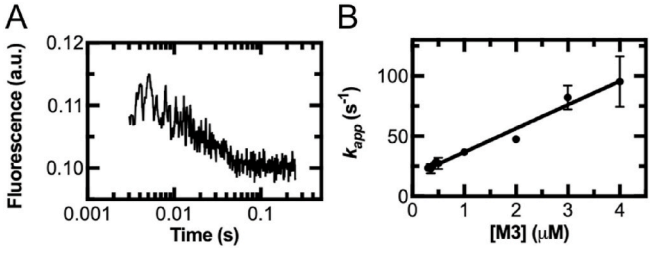

Fig. 4. Concentration dependence of the M3-association rate to MOS-detecting biosensor. (A) Representative fluorescence time-course of 2 μM M3 binding 100 nM MalX A134C-MDCC. (B) MalX A134C-MDCC (100 nM) fluorescence signal change across a variety of M3 concentrations (n = 4 for each data point, mean ± s.d.). When fit with a linear function the resulting slope yields an association rate constant of 20 ± 2 $\mu M^{-1}s^{-1}$ (n = 9, best fit ± s.d.).

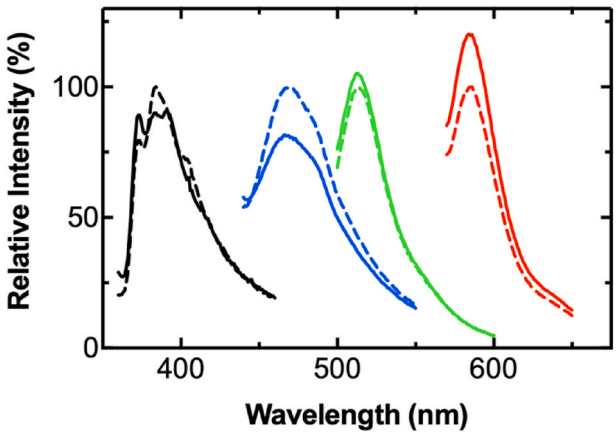

Fig. 5. MOS-detecting biosensor can be conjugated to a variety of fluorophores to alter fluorescence properties. Fluorescence emission spectra of MalX A134C conjugated to Pyrene (black), MDCC (blue), Fluorescein (green) or Rhodamine Red (red). Dashed spectra indicate MOS-detecting biosensor alone (20 nM), and solid spectra indicate MOS-detecting biosensor in the presence of MOS (10 μM). (For interpretation of the references to colour in this figure legend, the reader is referred to the Web version of this article.)

fluorophores gave a detectable response to M3 with changes in peak fluorescence intensity ranging from 5 to 29%, where differences in the magnitude of the reported fluorescence changes are likely due to the different shapes/sizes of the utilized fluorophores probing slightly different environments. MalX A134C labeled with dansyl (which is capable of forming a FRET pair with tryptophan) also reported a fluorescence change upon M3 addition after excitation of tryptophan at 280 nm (Table S2), thereby expanding the spectral range of our MOS-biosensor set to report emission maxima of 380 nm–580 nm. Together, these results demonstrate that a wide variety of fluorophores can probe the altered environment detected via our CINC pipeline, enabling rapid development of biosensor libraries with variable spectroscopic properties facilitating multiplexing of such assays.

3.6. Detection of MOS released from α-amylase-catalyzed starch degradation using MalX A134C-MDCC

To examine the utility of MalX A134C-MDCC in characterizing enzyme activity, we examined formation of MOS in real-time via *Bacillus licheniformis* α-amylase-catalyzed degradation of starch. Using the stopped-flow technique, all experimental conditions with α-amylase resulted in a time-dependence of the observed fluorescence signal decrease slower than the rate of M3 binding to MalX A134C-MDCC (Fig. 6A). The observed apparent rate of MOS generation is dependent on α-amylase concentration and fitting this dependence with a linear equation revealed a rate constant of 0.7 ± 0.1 $\mu M^{-1}min^{-1}$ (Fig. 6B), while the amplitude of the signal change was independent of α-amylase concentration (Fig. 6C). To demonstrate portability of our MalX A134C-MDCC biosensor to different detection platforms, we demonstrate that the kinetics of the α-amylase concentration-dependent rate can also be determined using a commonly used microplate reader assay (Fig. 6D). In agreement with our stopped-flow assay, the apparent rate of MOS generation is dependent on α-amylase concentration and fitting with a linear function yielded a rate constant of 1.4 ± 0.5 $\mu M^{-1}min^{-1}$ (Fig. 6E), while the amplitude of the signal change was independent of α-amylase concentration (Fig. 6F). Together, these findings demonstrate the utility of the CINC-designed MalX A134C-MDCC biosensor in detecting MOS release as part of coupled enzymatic assays enabling the characterization of the functional cycle of α-amylase.

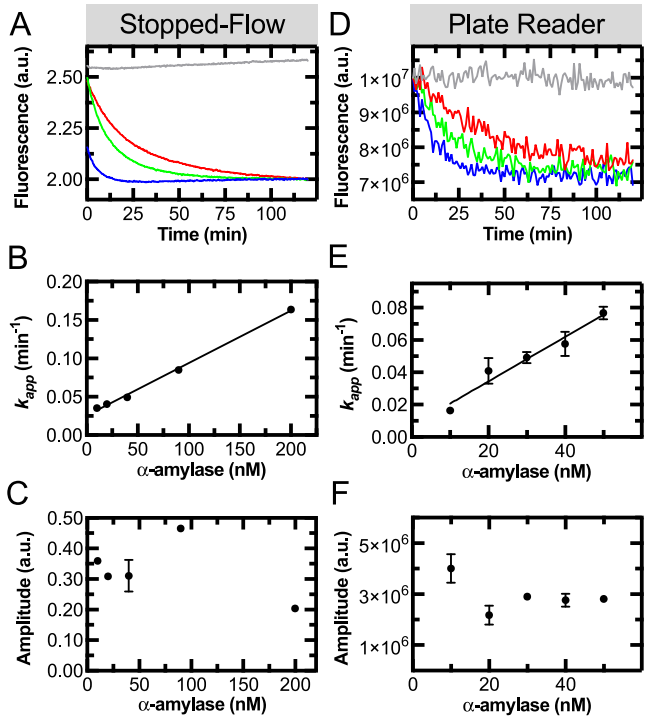

Fig. 6. MOS-release from α-amylase-catalyzed starch de-polymerization reported by MOS-detecting biosensor. (A) Representative fluorescence-time courses of MalX A134C-MDCC (1.5 μM) in the presence of 100 mg/L starch and α-amylase (0 nM, grey; 40 nM, red; 90 nM, green; 200 nM, blue) using the stopped-flow method. (B) Concentration dependence of α-amylase on the apparent rate (k_{app}) using a stopped-flow assay, MOS release into solution occurs with a rate constant of 0.7 ± 0.1 μM^{-1}min^{-1} (error reflects 95% c. i. in fit). (C) Amplitudes of MalX signal change remain constant as a function of α-amylase concentration using the stopped-flow method. (D) Representative fluorescence-time courses of MalX A134C-MDCC (1.5 μM) in the presence of 100 mg/L starch and α-amylase (0 nM, grey; 10 nM, red; 30 nM, green; 50 nM, blue) using a microplate reader. (E) Concentration dependence of α-amylase on apparent rate (k_{app}) using a microplate reader assay, MOS release into solution occurs with a rate constant of 1.4 ± 0.5 μM^{-1}min^{-1} (error reflects 95% c. i. in fit). (F) Amplitudes of MalX signal change remain constant as a function of α-amylase concentration using microplate reader assay (n = 3 for each data point, error bars on individual data points represent s.d.). (For interpretation of the references to colour in this figure legend, the reader is referred to the Web version of this article.)

4. Discussion

Due to the vast structural and functional diversity of carbohydrates found in nature the up-front costs of biosensor development using conventional approaches has limited the access to such advanced sensors for the majority of targets. However, to determine substrate specificity and kinetics of a CAZyme, suitable assays must be available. Commonly, carbohydrate activity assays are often laborious, involve non-continuous steps (i.e. manual sampling and/or downstream chemical derivatization), non-specific (i.e. detect many carbohydrates at once) or are linked (i.e. depend on other enzymes or cofactors) and don't lend themselves well to high-throughput or multiplexing. Biosensor-based assays for real-time, specific detection of target carbohydrates will be advantageous and pivotal for unlocking the detailed enzymatic characterization of genome-encoded CAZymes (the CAZome). The CINC pipeline employed here allows researchers to circumvent these limitations by enabling a rapid computer aided design and screening step to identify promising target positions for the subsequent introduction of fluorescence reporter groups, overcoming a critical hurdle for the streamlined (accelerated) and routine construction of novel biosensors for detection of user-defined reaction products.

As a proof of concept, we have demonstrated the utility of the CINC pipeline for the rational design of a novel biosensor capable of detecting M3. Of the four positions initially selected in MalX for substitution and subsequent fluorescent labeling based on their F_{Score}, two resulted in biosensors that gave a response to M3. Therefore, our current algorithm has a 50% success rate in identifying labeling positions that do not influence ligand binding properties. The described approach greatly minimizes time and cost of developing efficient, specific, and sensitive biosensors. As such the CINC-based design platform likely outperforms conventional approaches for developing protein-fluorophore conjugates, which produce biosensors that respond to the desired ligand in 20–30% of designs – often with altered binding affinity when compared to the unmodified protein (e.g. as in (Brune et al., 1994; De Lorimier et al., 2002)). As well, the fluorescent labeling sites selected by CINC are unique compared to conventional approaches. For example, in static crystal structures of both *apo* and MOS-bound MalX (PDB 2XD2 and 2XD3), position A134 adopts a loop secondary structure. However, our short molecular dynamics simulations suggest that position 134 in *apo* MalX adopts a secondary structure that exists in equilibrium between an α-helix and a loop conformation (Fig. 1C). It is therefore beneficial to utilize CINC to highlight changes in local dynamics that otherwise would go unnoticed using conventional approaches. The CINC pipeline will have broad applicability for biosensor design, as it is based on first-principles which in turn can be examined in a large number of biomolecules. However, additional testing with different protein scaffolds (data not shown) will further demonstrate the flexibility (i.e. general applicability to different protein scaffolds/adaptability to different input signals) of the scoring algorithm. Results for the four tested MalX variants will enable improved selection criteria for the development of future biosensors utilizing the CINC pipeline, whereby parameters used to calculate F_{Score} can be weighed differently guided by the success/failure of candidate biosensors response to ligand. For example, the largest contributor to F_{Score} for position 134 in MalX are changes in dihedral angles – suggesting future iterations of CINC could emphasize changes in dihedral in the F_{Score} criteria. A future iteration of CINC prioritizing changes in backbone dihedral angles may also improve the success rate of the algorithm, as large-scale changes in backbone dihedral angles were only seen in the successful candidate labeled at position 134 (Fig. 1B–D). As well, further optimization of F_{Score} cut-off values may improve selection criteria in future iterations of CINC. For example, this report used F_{score} values > 1.5 which led to successful biosensor designs utilizing positions T249C and A134C for fluorophore conjugation. However, it may be possible to enhance selection criteria with a more stringent F_{Score} cut-off (e.g. $F_{Score} > 2.5$).

In addition to streamlining the identification and selection of non-disruptive labeling positions in a protein of interest remote from the ligand binding site, the successfully identified positions are also robust with respect to fluorophore selection. MalX A134C conjugated with various environmentally sensitive fluorophores was able to report M3 binding at different wavelengths across the visible spectrum. This highlights an additional advantage of the CINC pipeline over previously developed labeling approaches, as many non-CINC developed biosensors heavily favor a specific protein-fluorophore combination to provide detection of a molecule of interest (e.g. as in (Brune et al., 1994; De Lorimier et al., 2002)), whereas CINC has identified an altered environment that can be reported by a wide variety of fluorescent groups with different spectral properties. Therefore, our system lends itself to rapid construction of biosensors with user-defined spectroscopic properties and may be easily amenable to development of multiplexed biosensor assays due to the lack of a strong fluorophore preference in CINC-developed biosensors. Such multiplexed biosensor assays would be desirable in a number of situations. For example, the detection of multiple carbohydrate ligands in complex mixtures of enzymes or microbes would be possible. In principle, this will enable evaluation of how

multiple substrates are being processed simultaneously in environments such as the gut microbiome or in biofuel feedstocks.

With respect to the developed MOS-detecting biosensor, the fluorophore conjugation site was selected via small-scale changes in local dynamics distal from the MOS binding site. The kinetic properties of ligand binding for MalX A134C-MDCC are similar to previously developed phosphate-detecting biosensors based on *E. coli* phosphate binding protein (Table S3) (Brune et al., 1994; Okoh et al., 2006; Smith et al., 2017) which has enabled detailed kinetic analysis of the timing and role of phosphate release in various systems (Kothe and Rodnina, 2006; Muretta et al., 2015; Savelsbergh et al., 2005; Smith et al., 2017). In the current study, we examine MOS-release from *B. licheniformis* α-amylase via our MOS-detecting biosensor. Because our MOS-detecting biosensor binds MOS rapidly and with high affinity, we propose that the observed fluorescence change by the MOS-detecting biosensor is rate-limited by the availability of free MOS in solution produced via starch de-polymerization and subsequent dissociation of the formed MOS from the starch degrading enzyme. Because of the non-destructive measurement of MOS in real time, when combined with information about the chemical step of glyosidic bond cleavage (e.g. obtained via quench flow), these biosensors can be used to characterize the contributions of the cleavage step and the timing of product release to the overall reaction cycle. Using prior approaches critical information about the catalysis and product release step cannot be deconvoluted, whereas our biosensor-based approach enables characterization of de-polymerization enzymes and their rational design, optimizing catalysis of de-polymerization relative to product release. The protein scaffold MalX is capable of binding MOS with degree of polymerization of 3–9 with similar affinity (Abbott et al., 2010), so it is likely that MalX A134C-MDCC similarly detects MOS with degrees of polymerization 4–6 and 8–9 in addition to the detection of M3 and maltoheptaose reported here. Together, the development of biomolecular tools like the MOS-detecting biosensor will provide an alternative solution to detect and discern between the formation of nascent carbohydrate in real-time and enable rapid characterization of CAZymes, including their enzymatic properties.

5. Conclusion

We describe the CINC platform for development of novel protein-fluorophore conjugates capable of responding to an input signal, such as ligand binding, by changing their fluorescence intensity. CINC exploits small-scale changes in amino acid dynamics for biosensor design, which is advantageous for the design of biomolecular tools that do not undergo large-scale global conformational changes upon ligand binding. An additional advantage of CINC over conventional biosensor design approaches is that it does not rely on locating the fluorescent reporter group in close proximity to the ligand binding site, which often leads to proteins with altered binding properties relative to the wild-type protein (ultimately leading to a smaller number of failed sensor designs). The CINC pipeline is rapid, and in most cases the time from conceptualization over final biosensor design and validation is less than one week. At this time, CINC uses high-resolution structural data for the protein scaffold in its *apo* and ligand-bound state. However, expansion of biosensor libraries using CINC can be further accelerated by coupling with next-generation protein structure modeling (Kuhlman and Bradley, 2019) thereby circumventing the requirement for high-resolution structural data and increasing the number of protein scaffolds accessible to CINC by orders of magnitude.

Funding

This work was supported by NSERC Discovery Grant (RGPIN-2016-05199), and Alberta Innovates Strategic Research Chair(SC60-T2) and Alberta Innovates Strategic Project Grant (G2018000211) to HJW, and AAFC funding (J-001589) awarded to DWA. DDS received an Alberta Innovates Graduate Student Scholarship and a University of Lethbridge School of Graduate Studies Tuition Scholarship. DG received an Alberta Innovates Graduate Student Scholarship and a University of Lethbridge School of Graduate Studies Tuition Scholarship.

CRediT authorship contribution statement

Dustin D. Smith: Conceptualization, Methodology, Software, Validation, Formal analysis, Investigation, Resources, Data curation, Writing – original draft, Writing – review & editing, Visualization. **Dylan Girodat:** Conceptualization, Methodology, Software, Formal analysis, Investigation, Data curation, Writing – original draft, Writing – review & editing, Visualization. **D. Wade Abbott:** Conceptualization, Resources, Writing – original draft, Writing – review & editing. **Hans-Joachim Wieden:** Conceptualization, Methodology, Resources, Writing – original draft, Writing – review & editing, Supervision, Funding acquisition.

Declaration of competing interest

The authors declare that they have no known competing financial interests or personal relationships that could have appeared to influence the work reported in this paper. DDS, DG, DWA, and HJW are joint inventors on International PCT Patent Application No. CA 2021/050110 (Filed January 30, 2021) which covers the CINC method for biosensor development.

Acknowledgements

This research was in part enabled by support provided by WestGrid (www.westgrid.ca) and Compute Canada (www.computecanada.ca). We thank the University of Lethbridge for the use of SynBridge (Lethbridge, AB, Canada), which was used for fluorescence plate reader experiments. We would like to thank Dr. Ute Kothe for the use of the fluorescence spectrophotometer, Dr. Ata Ghavidel for critical feedback on MOS-release assays, and Emily Wilton for critical reading of the manuscript.

Appendix A. Supplementary data

Supplementary data to this article can be found online at https://doi.org/10.1016/j.bios.2021.113899.

References

Abbott, D.W., Higgins, M.A., Hyrnuik, S., Pluvinage, B., Lammerts van Bueren, A., Boraston, A.B., 2010. Mol. Microbiol. 77 (1), 183–199.
Ashkenazy, H., Abadi, S., Martz, E., Chay, O., Mayrose, I., Pupko, T., Ben-Tal, N., 2016. Nucleic Acids Res. 44 (W1), W344–W350.
Belousov, V.V., Fradkov, A.F., Lukyanov, K.A., Staroverov, D.B., Shakhbazov, K.S., Terskikh, A.V., Lukyanov, S., 2006. Nat. Methods 3 (4), 281–286.
Berg, J., Hung, Y.P., Yellen, G., 2009. Nat. Methods 6 (2), 161–166.
Bianchi-Smiraglia, A., Rana, M.S., Foley, C.E., Paul, L.M., Lipchick, B.C., Moparthy, S., Moparthy, K., Fink, E.E., Bagati, A., Hurley, E., 2017. Nat. Methods 14 (10), 1003.
Brune, M., Hunter, J.L., Corrie, J.E., Webb, M.R., 1994. Biochemistry 33 (27), 8262–8271.
Celniker, G., Nimrod, G., Ashkenazy, H., Glaser, F., Martz, E., Mayrose, I., Pupko, T., Ben-Tal, N., 2013. Isr. J. Chem. 53 (3-4), 199–206.
Chen, T.-W., Wardill, T.J., Sun, Y., Pulver, S.R., Renninger, S.L., Baohan, A., Schreiter, E. R., Kerr, R.A., Orger, M.B., Jayaraman, V., Looger, L.L., Svoboda, K., Kim, D.S., 2013. Nature 499 (7458), 295–300.
Ciftci, D., Huysmans, G.H., Wang, X., He, C., Terry, D., Zhou, Z., Fitzgerald, G., Blanchard, S.C., Boudker, O., 2020. Sci. Adv. 6 (22), eaaz1949.
De Laurentiis, E.I., Mercier, E., Wieden, H.-J., 2016. J. Biol. Chem. 291 (44), 23136–23148.
De Lorimier, R.M., Smith, J.J., Dwyer, M.A., Looger, L.L., Sali, K.M., Paavola, C.D., Rizk, S.S., Sadigov, S., Conrad, D.W., Loew, L., 2002. Protein Sci. 11 (11), 2655–2675.
Edwards, K.A., 2021. Talanta Open, p. 100038.
Fonin, A., Povarova, O., Staiano, M., D'Auria, S., Turoverov, K., Kuznetsova, I., 2014. Opt. Mater. 36 (10), 1676–1679.
Fu, Y., Finney, N.S., 2018. RSC Adv. 8 (51), 29051–29061.

Gasteiger, E., Hoogland, C., Gattiker, A., Duvaud, S.e., Wilkins, M.R., Appel, R.D., Bairoch, A., 2005. The Proteomics Protocols Handbook, pp. 571–607.
Gilardi, G., Zhou, L.Q., Hibbert, L., Cass, A.E., 1994. Anal. Chem. 66 (21), 3840–3847.
Girodat, D., Mercier, E., Gzyl, K.E., Wieden, H.-J., 2019. J. Am. Chem. Soc. 141 (26), 10236–10246.
Hanes, J.W., Chatterjee, D., Soriano, E.V., Ealick, S.E., Begley, T.P., 2011. Chem. Commun. 47 (8), 2273–2275.
Harrison, M., Dunlop, M., 2012. Front. Microbiol. 3, 360.
Hsieh, H.V., Sherman, D.B., Andaluz, S.A., Amiss, T.J., Pitner, J.B., 2012. J. Diabetes Sci. Technol. 6 (6), 1286–1295.
Ispas, C.R., Crivat, G., Andreescu, S., 2012. Anal. Lett. 45 (2–3), 168–186.
Ko, W., Kim, S., Lee, H.S., 2017. Org. Biomol. Chem. 15 (41), 8761–8769.
Ko, W., Kim, S., Lee, S., Jo, K., Lee, H.S., 2016. RSC Adv. 6 (82), 78661–78668.
Kothe, U., Rodnina, M.V., 2006. Biochemistry 45 (42), 12767–12774.
Kuhlman, B., Bradley, P., 2019. Nat. Rev. Mol. Cell Biol. 20 (11), 681–697.
Kunzelmann, S., Webb, M.R., 2009. J. Biol. Chem. 284 (48), 33130–33138.
Kunzelmann, S., Webb, M.R., 2010. ACS Chem. Biol. 5 (4), 415–425.
Law, J.W.-F., Ab Mutalib, N.-S., Chan, K.-G., Lee, L.-H., 2015. Front. Microbiol. 5, 770.
Lombard, V., Golaconda Ramulu, H., Drula, E., Coutinho, P.M., Henrissat, B., 2013. Nucleic Acids Res. 42 (D1), D490–D495.
Markets, and Markets, 2019. Biosensors Market by Type (Sensor Patch and Embedded Device), Product (Wearable and Nonwearable), Technology (Electrochemical and Optical), Application (POC, Home Diagnostics, Research Lab, Food & Beverages), and Geography - Global Forecast to 2024, pp. 1–90.
Marvin, J.S., Schreiter, E.R., Echevarría, I.M., Looger, L.L., 2011. Proteins 79 (11), 3025–3036.
Marvin, J.S., Shimoda, Y., Magloire, V., Leite, M., Kawashima, T., Jensen, T.P., Kolb, I., Knott, E.L., Novak, O., Podgorski, K., 2019. Nat. Methods 16 (8), 763–770.
Mehrotra, P., 2016. J. Oral Biol. Craniofacial Res. 6 (2), 153–159.
Mercier, E., Girodat, D., Wieden, H.-J., 2015. Sci. Rep. 5, 7677.
Muretta, J.M., Rohde, J.A., Johnsrud, D.O., Cornea, S., Thomas, D.D., 2015. Proc. Natl. Acad. Sci. U.S.A. 112 (46), 14272–14277.
Okoh, M.P., Hunter, J.L., Corrie, J.E., Webb, M.R., 2006. Biochemistry 45 (49), 14764–14771.
Pardee, K., Green, Alexander A., Ferrante, T., Cameron, D.E., DaleyKeyser, A., Yin, P., Collins, James J., 2014. Cell 159 (4), 940–954.
Pardee, K., Green, A.A., Takahashi, M.K., Braff, D., Lambert, G., Lee, J.W., Ferrante, T., Ma, D., Donghia, N., Fan, M., 2016. Cell 165 (5), 1255–1266.
Polaina, J., MacCabe, A.P., 2007. Industrial Enzymes. Springer.
Rai, V., Acharya, S., Dey, N., 2012. J. Biomaterials Nanobiotechnol. 3 (2A), 315–324.
Rosler, K.S., Mercier, E., Andrews, I.C., Wieden, H.-J., 2015. J. Biol. Chem. 290 (30), 18650–18661.
Rurack, K., Resch-Genger, U., 2002. Chem. Soc. Rev. 31 (2), 116–127.
Salins, L.L., Goldsmith, E.S., Ensor, M.C., Daunert, S., 2002. Anal. Bioanal. Chem. 372 (1), 174–180.
Savelsbergh, A., Mohr, D., Kothe, U., Wintermeyer, W., Rodnina, M.V., 2005. EMBO J. 24 (24), 4316–4323.
Schneider, C.A., Rasband, W.S., Eliceiri, K.W., 2012. Nat. Methods 9 (7), 671–675.
Shin, H.J., 2011. Appl. Microbiol. Biotechnol. 89 (4), 867–877.
Smith, D.D., Girodat, D., Wieden, H.-J., Selinger, L.B., 2017. Anal. Biochem. 537, 106–113.
Solscheid, C., Kunzelmann, S., Davis, C.T., Hunter, J.L., Nofer, A., Webb, M.R., 2015. Biochemistry 54 (32), 5054–5062.
Srilatha, B., 2011. J. Nanomed. Nanotechnol. 2 (7), 1–5.
Tian, Y., Cuneo, M.J., Changela, A., Höcker, B., Beese, L.S., Hellinga, H.W., 2007. Protein Sci. 16 (10), 2240–2250.
Toseland, C.P., 2013. J. Chem. Biol. 6 (3), 85–95.
Verma, N., Bhardwaj, A., 2015. Appl. Biochem. Biotechnol. 175 (6), 3093–3119.
Webb, A.J., Homer, K.A., Hosie, A.H., 2008. J. Bacteriol. 190 (1), 168–178.
Yu, Z., Cai, G., Liu, X., Tang, D., 2021. Anal. Chem. 93 (5), 2916–2925.
Zeng, R., Wang, W., Chen, M., Wan, Q., Wang, C., Knopp, D., Tang, D., 2021. Nano Energy 82, 105711.
Zhang, K., Lv, S., Lin, Z., Li, M., Tang, D., 2018a. Biosens. Bioelectron. 101, 159–166.
Zhang, K., Lv, S., Lu, M., Tang, D., 2018b. Biosens. Bioelectron. 117, 590–596.